

CNT forest self-assembly insights from in-situ ESEM synthesis

Ramakrishna Surya ^a, Gordon L. Koerner ^a, Taher Hajilounezhad ^a, Kaveh Safavigerdini ^b, Martin Spies ^a, Prasad Calyam ^b, Filiz Bunyak ^b, Kannappan Palaniappan ^b, Matthew R. Maschmann ^{a,c,*}

^a University of Missouri, Department of Mechanical and Aerospace Engineering, Columbia, MO, 65211, USA

^b Department of Electrical Engineering and Computer Science, Columbia, MO, 65211, USA

^c MU Materials Science and Engineering Institute, Columbia, MO, 65211, USA

ARTICLE INFO

Keywords:

Carbon nanotube
Synthesis
In-situ

ABSTRACT

Understanding and controlling the dynamic self-assembly mechanisms of carbon nanotube (CNT) forests is necessary to advance their technological impact. Here, in-situ environmental scanning electron microscope (ESEM) chemical vapor deposition (CVD) synthesis observes in real time the real-time nucleation, assembly, delamination, and self-termination of dense ($> 10^9$ CNT/cm²), tall (> 100 μm) CNT forests. Forest synthesis is continuously observed from nucleation to self-termination. Assembly forces generated near the substrate detach CNTs from the substrate, which simulation suggests requires between 3 and 12 nN of tensile force. Delamination initiates at both the CNT-catalyst and the catalyst-substrate interfaces, indicating multiple delamination mechanisms. Digital image correlation applied to SEM image sequences measures time-invariant strain within growing forests, indicating that forests grow as rigid bodies after liftoff. The Meta CoTracker algorithm measured CNT growth rates reduce from 50 nm/s to full termination over 150 s. The kinematic behaviors we observe are foundational to understanding the process-structure-property relationships of CNT forests.

1. Introduction

CNT forests are electrically and thermally conductive, soft, durable, and are nearly perfect optical absorbers. The blend of mechanical, thermal, and electrical properties are advantageous in applications ranging from multifunctional structural materials [1,2], flexible sensors [3,4], electrochemical energy storage [5–7], electronics [8], and conductive interface materials [8,9]. The physical properties of CNT forests are significantly diminished relative to those scaled from individual CNTs. For example, the elastic modulus of an individual CNT may exceed 1 TPa, whereas the modulus of CNT forests is on the order of 1–100 MPa [10,11]. The degradation in properties originates from the highly tortuous and disorganized morphology of CNTs within a forest. The mechanistic processes guiding CNT forest self-assembly, and thus their material properties, remain uncertain [4,10,12–19], and insights into the process-structure-property relationships of CNT forests are limited.

Measuring the dynamic morphology evolution of CNT forests during synthesis poses several challenges because of the small observation length scale (sub-μm), high synthesis temperatures (> 600 °C), and the

need for precise control of the chemical environment. Digital video acquisition of a growing CNT forest may be achieved by placing a digital camera in-line with the process tube of a conventional chemical vapor deposition system [20]. Such a system can measure CNT forest height with a resolution on the order of 20 μm. Laser reflectivity from CNT forests grown in cold-walled chemical vapor deposition (CVD) chambers have measured the time-resolved height of growing CNT forests with a resolution on the order of 10 nm [21], but the technique is limited to height measurements alone. In-situ small angle X-ray scattering (SAXS) can measure population-based metrics including diameter, alignment, and areal density [22,23], but not individual CNT-CNT interactions [24]. Assuming an X-ray beam diameter of 100 μm [22], SAXS measurements sample approximately 10^7 CNTs when interrogating a 1 × 1 cm CNT forest with an areal density of 10^9 CNT/cm². SAXS measurements have contributed greatly to the understanding of population-level forest morphology evolution, including a decreasing CNT population density and CNT alignment with increasing growth time. The mechanisms promoting these behaviors, however, are inaccessible using SAXS alone.

In-situ transmission electron microscope (TEM) synthesis methods,

* Corresponding author. University of Missouri, Department of Mechanical and Aerospace Engineering, Columbia, MO, 65211, USA.
E-mail address: maschmannm@missouri.edu (M.R. Maschmann).

by contrast, directly capture real-time CNT synthesis imagery for both isolated CNTs and small CNT populations [25–29]. TEM enables sub-nanometer imaging resolution and can acquire images on the order of 100–1000 frames per second. In-situ TEM synthesis is a cold-walled CVD process, wherein the observation region is comprised of an electron-transparent, thin-film heater. Reaction gases are supplied to the heated zone either through direct vapor delivery within an environmental TEM (ETEM) chamber [25,28] or within a hermetically sealed, electron-transparent chamber established within the sample holder [30–32]. Most in-situ TEM CNT syntheses have produced sparse and disorganized CNTs rather than dense and vertically oriented CNT forests. Such studies typically examined catalyst particle behavior during active CNT synthesis [28,30]. Example in-situ TEM synthesis results include the dynamic motion of CNT catalyst particles, which can become partially incorporated into the inner diameter of CNTs during synthesis [30,33]. As elucidated by atomic-scale in-situ TEM synthesis, the active catalyst particle is likely iron carbide (Fe_3C) [33]. Other studies have demonstrated the mobility of iron catalyst nanoparticles on the surface of CNTs during CNT forest synthesis [34]. While TEM provides unparalleled image resolution of active catalyst nanoparticles and emerging CNTs, its field of view is limited, thereby restricting the observation of CNT forest population dynamics. For three-dimensional growth of CNT forests, TEM produces projected images through the thickness of a forest, obscuring depth perception and making image interpretation of high-density CNT forests challenging [26]. A schematic representation of minimum temporal resolution and total spatial resolution of existing techniques is provided in Fig. 1.

Here, we investigate the real-time in-situ CNT forest synthesis and self-assembly using environmental scanning electron microscope (ESEM) technique on thin-film heating substrates similar to those used in TEM synthesis. ESEM observations capture CNT forest assembly across length scales ranging from individual CNTs ($< 10 \text{ nm}$) to global behaviors of growing CNT forest microstructures ($> 100 \mu\text{m}$). We observed the CNT forest assembly process at the edge of well-defined CNT forest micropillars to acquire unobstructed views of the relevant assembly processes. Image acquisition was acquired at one frame per 2 s at spatial resolutions comparable to conventional SEM imaging. By

using a magnification of 50–100 kx, we observed critical processes at the level of individual CNTs, including nucleation, initial CNT self-organization, variations in CNT orientation over time, CNT detachment from the growth substrate, and self-termination. Global CNT forest measurements of strain and growth rate were facilitated by digital image correlation (DIC) software, CNT area density was quantified by hand-crafted analysis methods, and the growth rate of individual CNTs during self-termination was measured using the Meta CoTracker algorithm. Adventitious carbon deposition, which is a common product of SEM imaging, played an unexpected vital role in promoting localized catalyst reduction and the formation of tall CNT forest micropillars. The CNT forests synthesized by in-situ ESEM synthesis closely resemble the areal and density of CNT forests synthesized by atmospheric pressure hot-walled CVD synthesis.

2. Experimental

2.1. Sample preparation

Prior to CNT forest synthesis, a heating substrate (Protochips) was plasma treated using glow discharge at a pressure of 2500 Pa with a current of 15 μA for 5 min. The catalyst film catalyst stack was comprised of 10 nm aluminum oxide and 2 nm iron by ion-beam sputtering (South Bay Technologies IBS/e) at a base pressure of $1 \times 10^{-5} \text{ Pa}$.

2.2. In-situ environmental scanning electron microscope CNT synthesis

The heating substrate was mounted in a Protochips Fusion 350 SEM stage operated within an FEI Quanta 600F environmental SEM. The MEMS-based heating substrates used in SEM experiments are identical to those used for TEM-based in-situ experiments. The substrate generates a uniform temperature region $50 \times 50 \mu\text{m}$ and exceeds the 3×3 array of holes etched into the heated zone (see Fig. 2). The ESEM chamber with the substrate was pumped overnight (approximately 15 h) to achieve a chamber pressure of approximately $8.5 \times 10^{-5} \text{ Pa}$. A cold finger was used to capture volatile impurities and water vapor. The cold finger tank was filled with a slurry of dry ice and acetone for 1 h prior to in-situ testing. Liquid nitrogen was not used in the cold finger because of its low boiling temperature of -195.8°C , which would freeze acetylene (-80.8°C) on contact. Dry ice sublimates at a temperature of -78.5°C , just above the freezing temperature of acetylene.

To begin synthesis, acetylene gas was used to purge the SEM chamber by cycling between 10 and 150 Pa for three cycles. Acetylene was supplied at a constant 5 psi (34,400 Pa) to the ESEM auxiliary gas inlet. A metering valve in the ESEM regulates the gas flow rate (on the order of 100 sccm) to maintain the appropriate chamber pressure. Prior to synthesis, the SEM chamber pressure was stabilized at 10 Pa. Heating was applied at a constant rate of 15°C per second from ambient temperature to the synthesis temperature of 625°C utilizing closed-loop temperature control. Thermal drift generated from the expansion of the substrate was manually corrected by stage translation and focus manipulation. Images were acquired at a rate of 30 frames per minute.

2.3. SEM carbon deposition

Controlled exposure of the catalyst film to carbon increases CNT yield by accelerating catalyst nanoparticle reduction and dewetting [29]. In our experiments, adventitious carbon was deposited by electron beam induced deposition [35]. Hydrocarbon species on the sample surface or in the SEM chamber interact with the electron beam, the species crosslink and deposit as “diamond-like” carbon on the substrate [36]. This carbon layer is common in SEM and is visible as a black box [37].

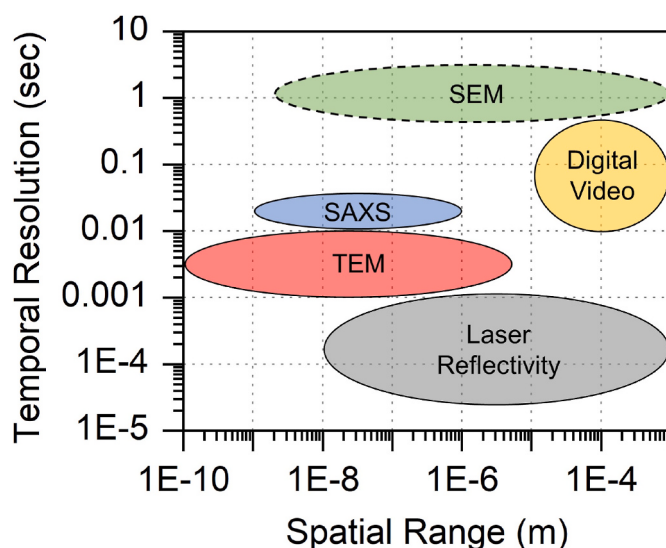


Fig. 1. Schematic mapping of various in-situ CNT forest synthesis measurement techniques. The applicable spatial domain of a technique is represented on the horizontal axis. The minimal temporal resolution is represented on the vertical axis. Of these techniques, only TEM and SEM can locally resolve individual CNTs and their dynamic behavior. Laser reflectivity and digital video measure the height of a CNT forest with time. SAXS resolves population-based distributions of CNT diameter, density, and alignment. (A colour version of this figure can be viewed online.)

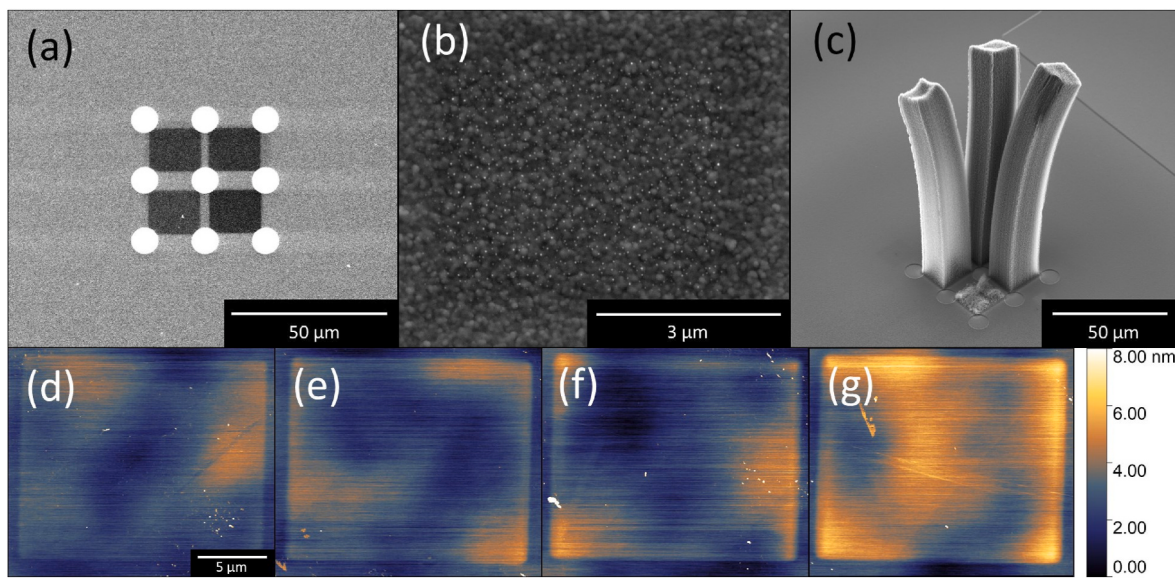


Fig. 2. Adventitious carbon deposition enabled patterned CNT synthesis. (a) SEM image of carbon deposition on a Protochips substrate using deposition times of 5, 10, 15, and 20 min. (b) SEM image of preferential reduction of an iron catalyst film when exposed to 550 °C in high vacuum. (c) SEM image of the CNT pillars from the substrate shown in (a). (d–g) AFM topology of adventitious carbon deposited on a silicon wafer using electron beam exposure times from 5 to 20 min, respectively. (A colour version of this figure can be viewed online.)

2.4. TEM analysis

After synthesis, the CNT forests grown using in-situ ESEM chemical vapor deposition were analyzed using TEM imaging and Raman spectroscopy. TEM samples were prepared by translating a TEM grid over the Protochips heated zone. CNTs were transferred to a lacey carbon TEM grid without solvent. TEM images were obtained using a JOEL JEM-1400 TEM at 120 keV acceleration voltage and a Gatan Rio 9 CMOS camera.

2.5. Raman spectroscopy

Micro-Raman spectra were acquired using a Renishaw InVia Raman microscope with 633 nm wavelength laser. Data were acquired between 100 and 2000 cm⁻¹ with an acquisition time of 30 s. Spectra were obtained directly on as-synthesized CNT forests on the Protochips heating substrate.

2.6. CNT forest synthesis simulation

A 3D mechanical finite-element simulation was modeled the interactions and forces generated during CNT forest growth and self-assembly, analogous to a 2D simulation previously reported [38–40]. In summary, the simulation treats CNTs as numerous interconnected frame elements, with evaluation nodes located at the terminal end of each element. A new element was added to the base of each CNT at discrete time steps to simulate CNT growth. CNT-CNT van der Waals interactions were modeled as linear-elastic spring elements. A global stiffness matrix consisting of all CNT elements and van der Waals elements was calculated at each time step prior to the addition of new CNT elements, and the displacement of all other nodes in the system is computed using the equation

$$F_t = [K_t]U_t - [K_{t-1}]U_{t-1} \quad (1)$$

where F_t is the external force vector, $[K]$ is the global stiffness matrix, U is the displacement vector, the subscript t refers to the current time, and the subscript $t - 1$ refers to the previous time step. This matrix equation was solved for each time step to compute the displacement vector, U_t , for all nodes in the system.

2.7. Digital image correlation

VIC-2D version 7 (Correlated Solutions, Inc.) software was used to evaluate the translation and strain of growing CNT forest pillars. The DIC evaluation criteria include 25 to 50-pixel evaluation subsets at 3–5 pixel steps. The low-pass filter was used to minimize the influence of image noise. The correlation algorithm utilized a 4-tap spline interpolation. A normalized squared differences method was used to accommodate potential changes in gray scale from image to image.

2.8. Meta CoTracker

The CoTracker algorithm [41] was implemented using Python 3.11 running on a NVIDIA Quadro RTX 8000 GPU. A total of 62 evaluation points were tracked throughout a sequence of 350 in-situ ESEM images. Evaluation points were within the field of view for approximately 10–15 frames, at which time the evaluation point no longer contributed data.

3. Results and discussion

3.1. Catalyst reduction, CNT nucleation, and early CNT growth

Prior to CNT synthesis, a catalyst iron thin film must undergo dewetting to transform into discrete catalytic nanoparticles. In our experiments, catalyst reduction and dewetting was spatially controlled by patterned adventitious carbon deposited by SEM electron beam rastering prior to substrate heating. Carbonaceous species, whether in gaseous or solid form, facilitate the efficient reduction of the iron thin film at low pressure, promoting the growth of dense CNT forests [29,42]. The carbon was deposited by repeatedly scanning the electron beam over the isolated regions targeted for patterned CNT forest growth for up to 20 min. These depositions were clearly visible in SEM imagery before the synthesis process, as illustrated in Fig. 2a. The array of dark squares represent varying levels of carbon deposition, as controlled by the duration of electron beam scanning. Upon heating, iron nanoparticles formed and appeared as a field of bright particles within the carbon deposition region, as depicted in Fig. 2b. A more detailed video of the dynamic formation of iron nanoparticles is available in the supplementary information video S1. The catalyst nanoparticles shown in 2b

were formed at a temperature of 550 °C in a high vacuum environment without the intent of CNT synthesis. Note that particle formation occurred below the CNT synthesis temperature of 625 °C. Dense CNT forest micropillars grew from the carbon deposition regions in Fig. 2a—as shown in Fig. 2c. CNT forests with heights exceeding 100 μm occurred within three of the four regions of carbon deposition, representing 10, 15, and 20 min of continuous electron beam carbon deposition. Only sparse CNT synthesis was observed in the region corresponding with the lowest carbon dose corresponding with 5 min of deposition. The nearly binary variation in CNT forest height indicates that a minimum dose of carbon is needed to support robust catalyst reduction and subsequent CNT forest synthesis. Numerous unsuccessful syntheses occurred in the absence of adventitious carbon, characterized by sparse or no observable CNT growth.

Atomic force microscope (AFM) topography images of adventitious carbon deposited on silicon wafers show the relationship between carbon deposition and electron beam scan time. The deposition regions shown in Fig. 2d-g employed the same SEM carbon deposition parameters used in Fig. 2a. The coverage area and thickness of the deposition increased with longer electron beam deposition times. The greatest carbon deposition often occurs near the boundaries of the scanned areas where electron beam scanning terminates, resulting in a non-uniform carbon topology within the deposition zone. It is unclear how the carbon migrates and distributes upon heating and catalyst dewetting. Nevertheless, it is evident that the patterning of carbon enabled well-defined activity of iron catalyst nanoparticles, which in turn enabled in-situ observation of well-defined CNT forest edges.

3.2. CNT forest assembly

The well-defined vertical faces of CNT forest pillars offered an ideal platform for observing the growth and assembly of CNTs at all magnifications. Individual CNT behaviors were readily discernible between 50,000–100,000 x magnification. The analysis of bulk, monolithic micro-pillar behavior was conducted at approximately 10,000 x magnification. High magnification examination demonstrated that the CNTs followed the base-growth mechanism, wherein the catalyst for CNT synthesis remained on the substrate during the growth process. This observation aligns with the findings of previous studies that employed similar catalyst systems.

The catalyst reduction and early CNT forest assembly obtained in a 10 Pa C₂H₂ environment is shown in Fig. 3. After 28 s of heating, bright catalyst nanoparticles formed at a temperature of 425 °C, signaling the dewetting of iron nanoparticles. Approximately 10 s later (575 °C), CNTs nucleated from a fraction of the visible catalyst particles. Early CNTs exhibited mainly an arched morphology, where the CNT tips and bases were in contact with the growth substrate. As the CNT arches lengthened, neighboring CNTs contacted each other due to crowding, forming van der Waals bonds between contacting CNTs. Contacting CNTs formed small assemblies that lifted away from the growth substrate. Over time

and with increased CNT growth, isolated assemblies merged together to form a fully connected CNT forest. The arching of CNTs at early stages of growth may contribute to the relatively high-density crust layer frequently found at the top surface of CNT forests. The early CNT-CNT assembly appeared similar to that observed by in-situ TEM CNT forest synthesis, where the density of CNT-CNT contacts significantly increased with time [26]. A video of the sequence in Fig. 3 can be found in supplemental information video S2.

After fully connected CNT forests formed, CNT-CNT and CNT-substrate interactions were observed at the edge of the micropillars. The mechanical degrees of freedom at the CNT base may be inferred by the change in orientation angle between a CNT and the substrate in response to mechanical loading. The deformation of CNTs allowed by this boundary condition plays a critical role in CNT forest morphology evolution, as it determines rotational mobility. A time-invariant orientation angle at the substrate would infer a fixed-end boundary condition that disallows CNT rotation. A time-varying angle would suggest that CNTs and/or catalyst particles can rotate or reconfigure in response to dynamic loads transmitted to the catalyst particles. We measured the projected rotation of four representative CNTs over 105 consecutive SEM imaging frames, corresponding to an observation of 210 s (Fig. 4b). The angle data demonstrates that CNTs are pre-dominantly oriented at an angle of approximately 90°, perpendicular to the growth substrate. Notably, CNTs labeled as CNT 1 and CNT 4 exhibit a nearly Gaussian angular distribution centered at 90°, while CNT 2 and CNT 3 show secondary peaks, indicating a secondary preferred orientation. The second orientation arose from repeated interactions between the measured CNT and a neighboring CNT. A time-resolved plot of CNT angle (Fig. 4c), demonstrates that the orientation angle of CNTs continuously vary, indicative of pinned mechanical boundary condition that permits rotation without translation. The rate of change in orientation angle between consecutive frames is depicted in Fig. 4d. A Gaussian fit to the cumulative frame-to-frame angle variation data generated by the four CNTs yields a mean angle change of 0.05° per frame and a standard deviation of 19.0° per frame. The average near zero degrees represents that the CNT oscillates at equal rates to the left and right relative to the observation frame. Occasional significant and abrupt changes in angle suggest that rapidly varying loads are transmitted to the CNT catalyst. The observed rotation may be accommodated by the CNT and catalyst system through CNT catalyst rotation about the substrate, catalyst reconfiguration, generation of CNT defects, CNT kinking, or rotation of the CNT about a fixed catalyst nanoparticle.

3.3. Pillar kinematics

After lifting from the growth substrate, CNT forest micropillar monoliths grow vertically away from the substrate. Digital image correlation (DIC) software was used to measure the collective CNT forest pillar growth rate, lateral translation, and internal strain. DIC algorithms evaluate pixel-by-pixel motion of a surface across an image sequence.

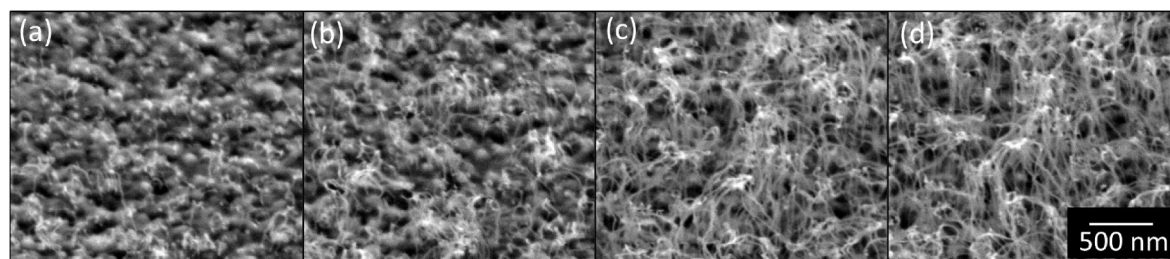


Fig. 3. Early stages of CNT forest self-assembly. An in-situ ESEM synthesis image sequence shows CNT growth at (a) t = 2, (b) t = 4 s, (c) t = 6 s and (d) t = 8 s after nucleation. (a) CNTs initially form arches along their length, with the base and tip contacting the substrate. Growth is independent of neighbors. (b) Upon achieving approximately 1 μm of growth, neighboring CNTs cling together via van der Waals force, forming (c) localized colonies of entangled and vertically oriented CNT tufts. Each tuft grows in height and breadth (d), eventually contacting neighboring colonies and forming a continuous CNT forest. (A colour version of this figure can be viewed online.)

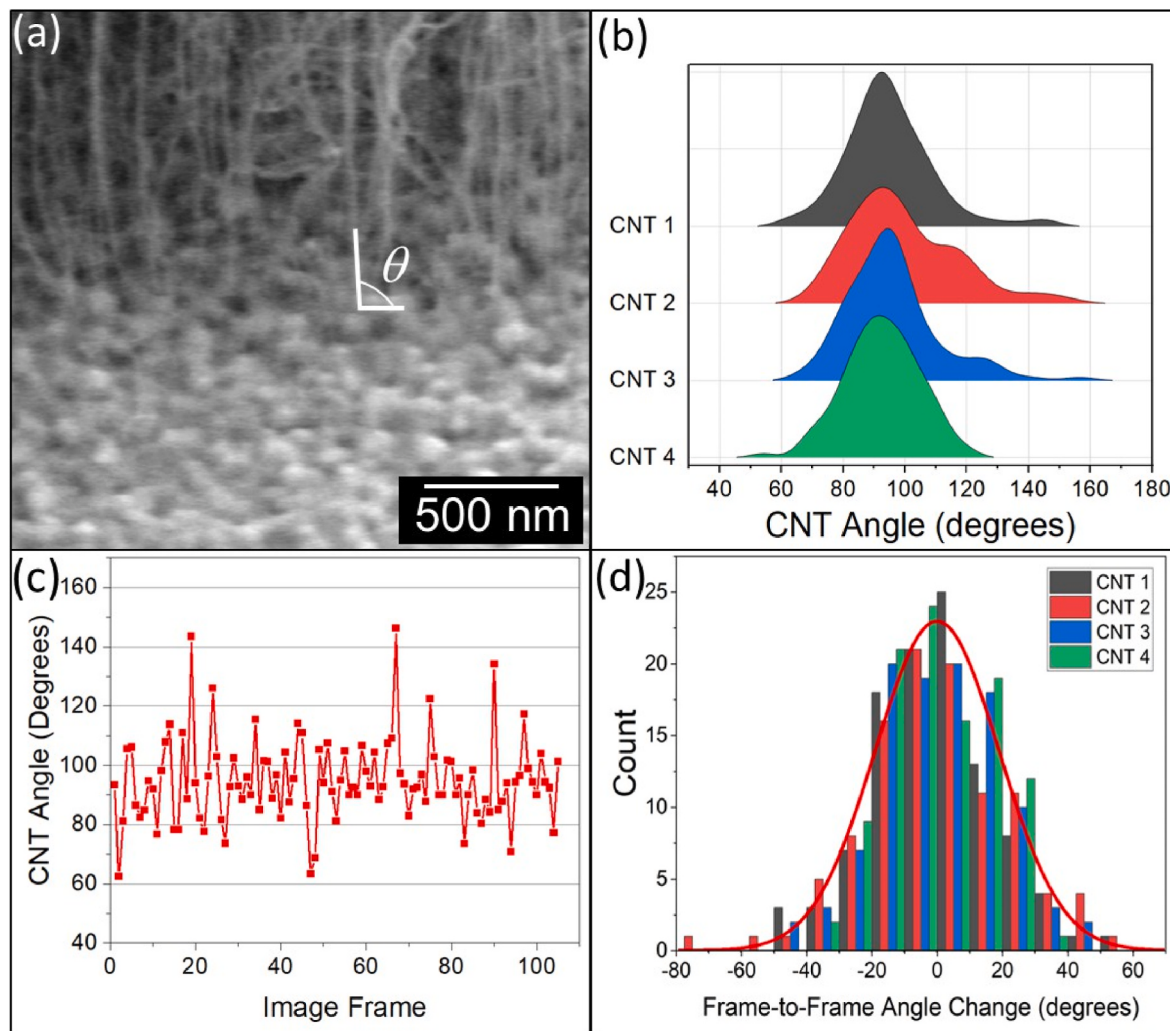


Fig. 4. Measuring the dynamic orientation angle of CNTs relative to the growth substrate. (a) Example measurement scheme, as measured from in-situ ESEM image sequences. (b) Time-averaged histograms of 4 CNTs obtained over 105 sequential images (210 s). (c) A representative time sequence of CNT orientation angle as a function of time. (d) A histogram of frame-to-frame angle variation for four CNTs and an overlaid Gaussian fit to the population data. (A colour version of this figure can be viewed online.)

Whereas a high-contrast speckle pattern is typically applied to surfaces to facilitate DIC measurements, the high-contrast pixel pattern generated by CNT forest SEM imagery is sufficient [43,44]. Fig. 5a shows a representative DIC evaluation frame imposed on a growing CNT pillar. The color contours in the DIC evaluation box represent vertical displacement contours. The pillar displayed in Fig. 5a was monitored for 630 image frames, corresponding to a total observation time of 21 min. The vertical displacement measured by DIC, displayed in Fig. 5b, exhibits an exponential growth rate decay with time. The initial growth rate of 110 nm/s was measured 14 s after nucleation, and it decreased to 40 nm/s towards the end of observation. The measurement was unable to measure the beginning 14 s of growth rate because finite time was required to acquire focus and reposition the area of interest because of sample drift. Previous CNT forest growth rate studies used laser displacement and cold-walled CVD with ethylene feedstock at atmospheric pressure and 1010–1120 °C growth temperatures. These measurements showed a rapidly increasing growth rate at the onset of CNT forest synthesis, followed by a steady decrease in growth rate, and abrupt self-termination [24]. Optical measurements of hot-walled CNT forest growth rates showed a similar trend [20]. While it is difficult to directly compare quantitative growth rate results between these experiments because of drastically different synthesis conditions, a decreasing CNT growth rate after initial rapid growth is consistent with prior

observation.

Lengthening CNT forest micropillars exhibited coordinated lateral oscillations, normal to the growth direction, in addition to their vertical growth. The DIC-measured oscillating behavior of a representative CNT forest pillar is exhibited in Fig. 5c, with a peak-to-peak lateral translation of up to 130 nm. The oscillations reflect mechanical competition between contacting CNTs lengthening at different growth rates. As vertical lengthening of fast-growing CNTs was resisted by slower growing CNTs, the excess length was accommodated by coordinated waviness that is frequently observed within CNT forests. These buckles originate just above the substrate and persist as the forest collectively grows vertically.

The internal CNT forest strain parallel to the growth direction, σ_{yy} , and normal to the growth direction, σ_{xx} , remained invariant at zero strain, as shown in Fig. 5d. A DIC evaluation window was first established just above the growth substrate as a CNT volume lifted free of the substrate. A consistent zero strain within the evaluation window indicates that mechanical strain is constant within a CNT forest after it lifts from the substrate, implying that the CNT forest acts as a rigid body. It is important to note that the strain measurement is relative to the strain state at which the DIC software first registered a consistent image speckle pattern, which occurred at about 1 μm above the substrate. Non-zero retained mechanical strain likely exists within the volume however,

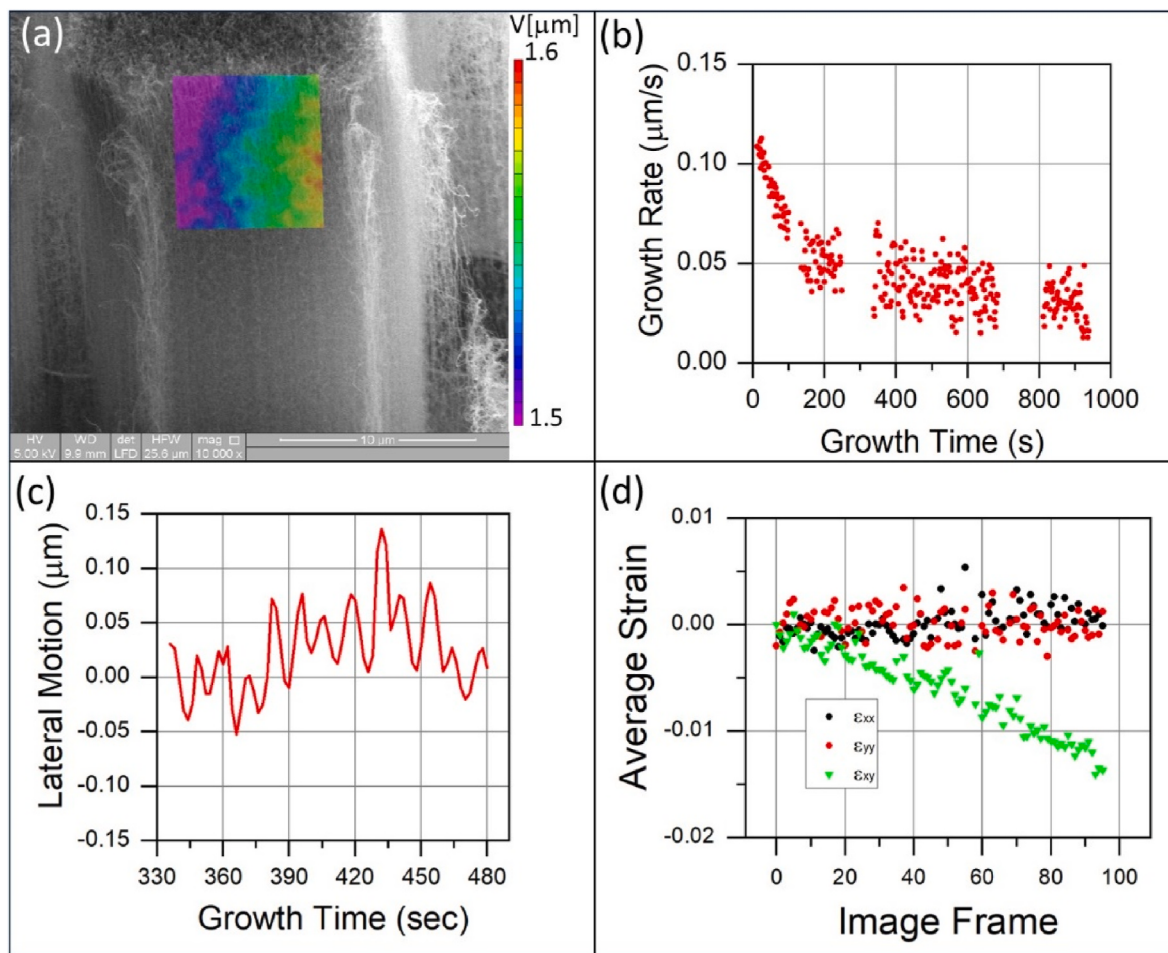


Fig. 5. Digital image correlation (DIC) analysis of in-situ ESEM CNT forest synthesis. (a) An in-situ CNT image overlaid with a DIC evaluation box measuring vertical displacement, V . (b) The average CNT forest vertical growth rate of the CNT forest pillar in (a) as a function of time obtained by averaging the vertical displacement within DIC evaluation boxes. (c) DIC measured lateral motion of the growing CNT forest pillar shown in (a). (d) DIC measured lateral (ϵ_{xx}), vertical (ϵ_{yy}), and shear strain (ϵ_{xy}) for the CNT pillar shown in (a). The constant ϵ_{xx} and ϵ_{yy} indicates that the pillar moves as a monolithic rigid body with invariant internal strain. Linearly decreasing shear strain is an indication that the CNT pillar is slowly growing at a tilted angle. (A colour version of this figure can be viewed online.)

evidenced by the tortuous CNT morphology. The DIC measurement indicates that the strain within the forest is retained and does not relax as a given volume travels farther from the substrate. A steadily decreasing shear stress, τ_{xy} , corresponded to the gradual bending of the pillar towards the left as it vertically grows upward. A representative DIC evaluation sequence video is shown in supplemental information video S3.

3.4. CNT delamination

A persistent temporal decrease in CNT areal density was observed for all CNT syntheses. Previous in-situ SAXS measurements showed that areal density decreased by approximately half within the first 200 μm of growth of CNT forests grown at atmospheric pressure [29]. In-situ ESEM provides sufficient spatiotemporal resolution to observe both the individual CNT detachment events that SAXS cannot discern and the CNT forest global density. Using ImageJ analysis software, a horizontal analysis line was projected across the field of view on image sequences, and the gray-scale pixel intensity profile was measured across the line (Fig. 6a). Each peak in intensity profile represented a CNT or small CNT bundle intersecting the boundary. The intensity peaks were identified and counted using the Peak Analyzer tool in Origin 2022 software. The density analysis encompassed a 200-s evaluation window beginning 66 s after the initiation of CNT growth. The 66 s duration represents the time required to focus and center the observation area after initial thermal

drift. The CNT density evolution is presented in Fig. 6b. The horizontal field width of the image sequence was 2.56 μm, and the depth of field was estimated to be 1 μm. The number of CNTs decreased from 74 in the first frame (66 s after CNT growth initiation) to 52 CNTs after 200 s, or approximately 20 μm of CNT forest growth. These CNT counts correspond to an absolute CNT density ranging from approximately 6×10^9 to 4×10^9 CNT/cm², respectively, consistent in scale with previous SAXS measurements [22,23]. Although the SEM cannot differentiate between individual CNTs from small CNT bundles, it provides a reasonable and consistent estimate of CNT density as a function of time.

Multiple CNTs were directly observed detaching from the growth substrate. Two such CNT detachment events are shown in Fig. 6c-f. Some CNT delamination events appeared to leave a catalyst particle adhered to the substrate (Fig. 6e-f), while others appeared to remove the catalyst particle from the substrate (Fig. 6c-d). The presence or absence of a catalyst particle provides insight into the detachment mechanism and the relative energy of adhesion. Detachment may occur between the CNT-catalyst particle interface or the catalyst particle-substrate interface according to the adhesion strength in those two regions. Prior adhesion tests of CNT forests conducted at room temperature observed that delamination events of as-grown CNT forests occur preferentially at the CNT-catalyst [45] or a mix of CNT-catalyst and catalyst-substrate delamination [46]. Though not explicitly discussed, particle-substrate detachment was observed in prior in-situ TEM studies [26] (see Supplementary Information). Our in-situ SEM observations indicate that a

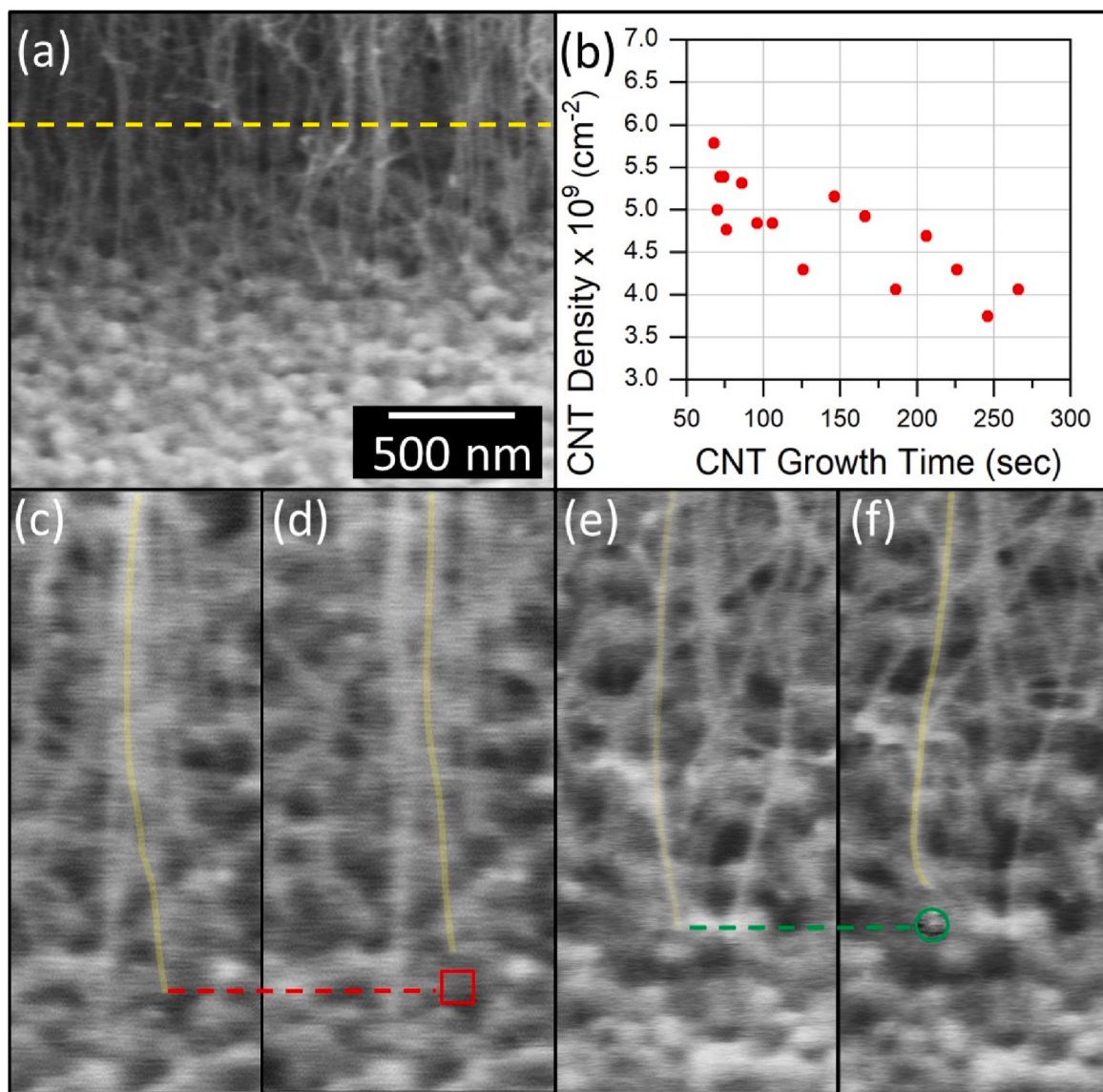


Fig. 6. Direct observation of CNT forest areal density decay. (a) The CNT areal density was measured by counting grayscale intensity peaks across a horizontal line overlaid to an in-situ ESEM image sequence. (b) The areal density decreased with synthesis time. Individual CNT detachment events, including (c–d) show CNT detachment at the catalyst-substrate interface. No catalyst particle is observed after CNT liftoff, as indicated by the square in (d). (e–f) Before and after images showing the detachment of a CNT at the CNT-catalyst interface, with the substrate-adhered catalyst particle circled in (f). The detached CNT is highlighted in yellow in both image sequences. These delamination events may also be observed in the Supplementary Information video S4. (A colour version of this figure can be viewed online.)

mix of both mechanisms are active at the elevated temperature of the synthesis environment. A video highlighting CNT detachment may be found in supplemental information video S4.

Utilizing a 3D mechanical finite element simulation, we quantified the forces conveyed to catalyst particles at the base of each CNT during CNT forest synthesis and self-assembly [38,40]. To ascertain the upper limits of anticipated CNT delamination force, the simulation postulated continuous substrate adhesion and the absence of CNT delamination. In this computational framework, all CNTs within the forest were characterized by an outer radius of 10 nm and an inner radius of 5 nm. Consistent with in-situ observations, CNT-CNT contacts were persistent once established. The CNT population growth rate reflected a log-normal distribution, with a population averaged growth rate of 60 nm per iteration and a standard deviation of 10 % of the mean. The simulation spanned a square region consisting of 100 x 100 CNTs at a density of $6 \times 10^9 \text{ CNT/cm}^2$ over 200 time steps, yielding a final CNT forest height of approximately 10 μm . A density $6 \times 10^9 \text{ CNT/cm}^2$ was

selected as a CNT density to be consistent with our experimentally observed initial areal densities (Fig. 6b).

A histogram depicting the axial force transmitted to the base of each CNT for all time steps is presented in Fig. 7a. Over the course of 200 simulated time steps, the maximum simulated force exerted between CNTs and the substrate ranged from +342 nN (tension) to -488 nN (compression). Previous work by Brown et al. [46] established a critical tensile loading threshold of 12 nN/CNT to delaminate a CNT forest from its substrate at room temperature. Others have estimated the delamination force of between 1 and 3 nN per CNT [45]. The simulated forces generated during self-assembly exceed these critical values by at least an order of magnitude, suggesting that delamination is likely during the synthesis process. Using 12 nN as a critical tensile load to activate delamination, 1460 unique CNTs, corresponding to 14.6 % of the CNT population, experienced sufficient force to delaminate through approximately 10 μm of CNT forest growth (200 time steps). A critical detachment force of 3 nN resulted in 2927 unique CNTs experiencing

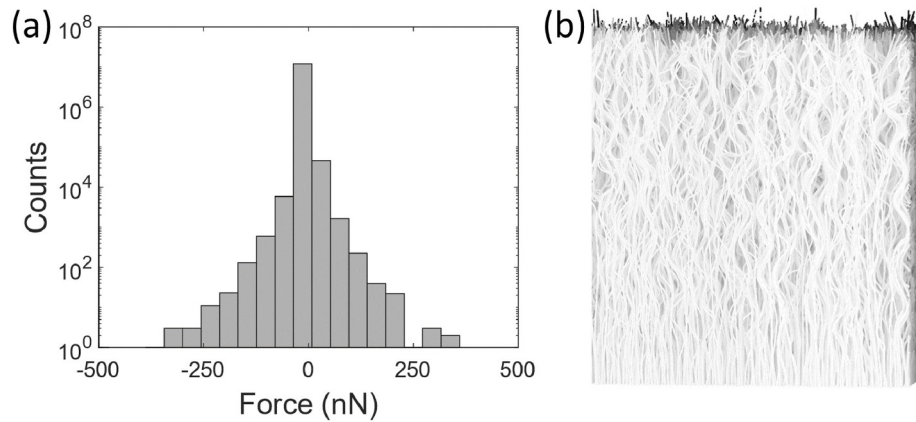


Fig. 7. A 3D mechanical finite element simulation evaluated the self-assembly force exerted at the CNT-substrate interface for 10,000 CNTs and approximately 10 μm of height. All CNTs were anchored to the growth substrate. (a) A histogram of the CNT-substrate force spanned from -488 nN (compression) to 342 nN (tension), with most recorded forces near zero load. (b) The resulting simulated CNT forest morphology resembles CVD-synthesized CNT forests. (A colour version of this figure can be viewed online.)

sufficient force to delaminate. Assuming CNT detachment would occur when the critical force is exceeded, the simulated density after 10 μm of CNT forest growth would range from $4.3\text{--}5.1 \times 10^9 \text{ CNT/cm}^2$ for 3 nN and 12 nN critical forces, respectively, in good agreement with the ESEM experimental observations shown in Fig. 6b. For reference, 10 μm of CNT growth corresponds to approximately 200 s in Fig. 6b. The consistency between mechanical simulation and experiment points to the

reaction forces generated during CNT self-assembly as a significant driver of CNT population decrease.

3.5. CNT forest self-termination

The self-termination of CNT forest growth typically occurred after approximately 20–30 min of synthesis. During self-termination, an

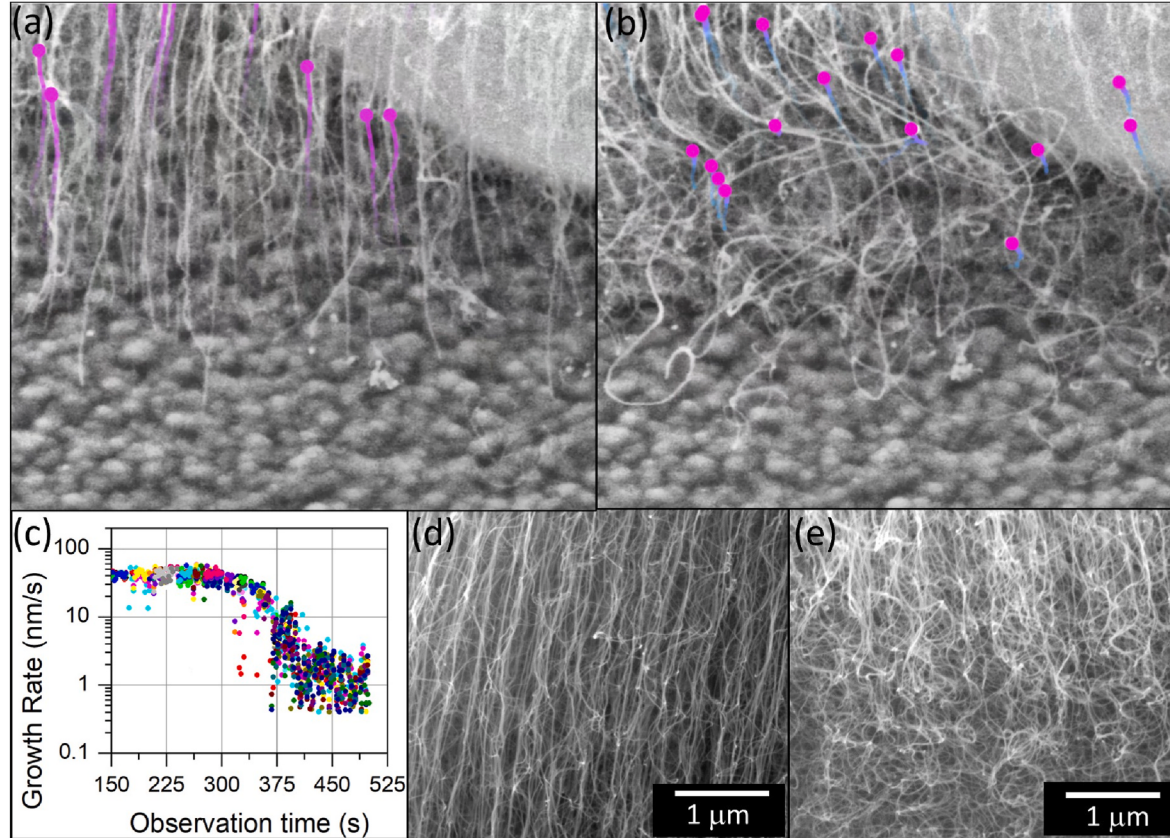


Fig. 8. In-situ ESEM images of CNT forest self termination. The motion path of CNT features were measured using the Meta CoTracker algorithm beginning (a) 150 s after CNT forest synthesis initiation to (b) self termination. The solid circles indicate the locations of evaluation points in the current frame, while the trailing tails represents time histories of the points. (c) The vertical growth rate is nearly constant between 40 and 50 nm/s at the beginning of the analysis, followed by a growth rate decay beginning at 300 s and an increased growth rate disparity between CNTs. SEM images obtained after self termination show general CNT alignment near the top of the forest, (d), and significant disorder at the bottom of the forest, (e), where the CNT population experienced self-termination. (A colour version of this figure can be viewed online.)

increasing fraction of CNTs rapidly cease growing, and the CNT forest height becomes static. The abrupt catalytic self-exhaustion of CNT forests has been experimentally measured by others using laser reflection measurements [24] or optical imagery [20]. In-situ TEM measurements of CNT forest self-termination are impractical because the CNTs themselves obscure the observation. Using in-situ ESEM synthesis, we observed that the activity of CNTs terminates in a distributed manner. The vertical growth of actively growing CNTs is resisted by CNTs that have stopped growing and are tethered to the substrate. Actively growing CNTs bend and buckle because of mechanical resistance, while the inactive, tethered CNTs experience a corresponding tensile force. The CNTs near the substrate exhibit a highly tortuous morphology because of this mechanical competition. The collective tensile load experienced by the inactive CNTs during this phase does not induce large-scale CNT delamination, indicating the load generated by active CNTs is well distributed among the inactive CNTs. The compressive load experienced by actively growing CNTs will transmit to the catalyst particle, where mechanochemical coupling may act to slow or deactivate catalyst activity [47].

The growth rate of CNTs before and during self-termination was evaluated using the Meta CoTracker algorithm, a transformer network that models the correlation of different points in time via specialised attention layers [41]. By tracking points identical points across an image sequence, the motion path of CNTs was determined. Near the initiation of CNT forest growth (Fig. 8a), the CNT path was largely vertical, normal to the growth substrate, and CNTs exhibited a high degree of alignment. The time history of evaluation points is represented by the tail of each point in Fig. 8a–b. During self termination (Fig. 8b), the growth of CNTs rapidly decelerated until most CNTs ceased growth, as observed by the shortened tails of evaluation points provided by CoTracker. The remaining active CNTs moved in a highly tortuous path because they were unable to advance in the vertical direction against the resistance of inactive CNTs. The growth rate observation began 150 s after the initiation of growth. The initial vertical growth rate 40–50 nm/s is consistent with previous measurements obtained by DIC and presented in Fig. 5. This growth rate was nearly constant for the observation time between 150 and 300 s. The CNT growth rate rapidly decreased thereafter, until ceasing at approximately 450 s. The relative disparity in growth rates also increased during self-termination, indicating that growth rates of CNTs within the population were decelerating at different rates. While the CoTracker algorithm readily tracked the motion path of slowly decelerating CNTs, it could not track the rapid and unpredictable tortuous path of active, rapidly growing CNTs at this phase; therefore, the most rapidly growing CNTs are not well reflected in the growth rate data in Fig. 8c. The difference in CNT forest tortuosity is readily observed when comparing images obtained near the top of the forest (Fig. 8d), which grew when CNTs were growing at a more uniform rate, to the morphology at the bottom (Fig. 8e) which underwent self

termination and a large disparity of CNT growth rates. A video of the CoTracker image sequence is found in supplementary information video S5.

3.6. Ex-situ CNT forest characterization

After synthesis, TEM images of CNTs were acquired across 28 different evaluation locations at magnification exceeding 150 kx. The inner and outer diameter of the CNTs were measured using imageJ software. A representative TEM image is shown in Fig. 9a. Multi-walled CNTs (MWCNTs) were observed, with concentric walls. Amorphous carbon was visible on the external surface of CNTs. Histograms of the inner and outer CNT diameter are shown in Fig. 9b, indicating an average diameter of 12.3 nm and inner diameter of 6.6 nm. The CNT diameter distribution is similar to that observed during cold-walled CVD SAXS synthesis [23,48].

The Raman spectra of as-grown CNT forests were obtained from freestanding CNT forest pillars supported on the Protochips substrate. Fig. 9c shows that the intensity ratio of the disordered carbon peak (D-peak) at approximately 1340 cm^{-1} to that of the well graphitized carbon peak at 1580 cm^{-1} is 1.1, similar to CNT forests grown using atmospheric CVD with a thin film catalyst [49,50].

4. Conclusion

The evolving stages of CNT forest growth, including nucleation, self-assembly, delamination, and self-termination were directly observed using in-situ ESEM synthesis. The technique facilitated observation of the nucleation and delamination of individual CNTs while also enabling quantification of mesoscale translation and strain using digital image correlation (DIC). Near the growth substrate, mechanical competition between CNTs growing at desperate rates acted to deform contacting CNTs and delaminate slower-growing CNTs from the growth substrate. We observed delamination at both the CNT-catalyst and the catalyst-substrate interfaces. Simulation of growing CNT forests show that the forces transmitted to the growth substrate can greatly exceed the 3–12 nN tensile force required to induce delamination of CNT forests at room temperature post-synthesis, suggesting that these forces were likely a primary cause for CNT delamination. A few microns above the growth substrate, beyond the height of new CNT-CNT contact formation, DIC analysis showed that growing CNT forests acted as rigid bodies. The CNT assembly behaviors observed by ESEM govern the collective structure and properties of CNT forests. In-situ ESEM synthesis, with complementary in-situ TEM, advanced image analysis, and dynamic simulations, is expected to continuously advance the mechanistic understanding of CNT forest synthesis towards the goal of tailored CNT forest property sets.

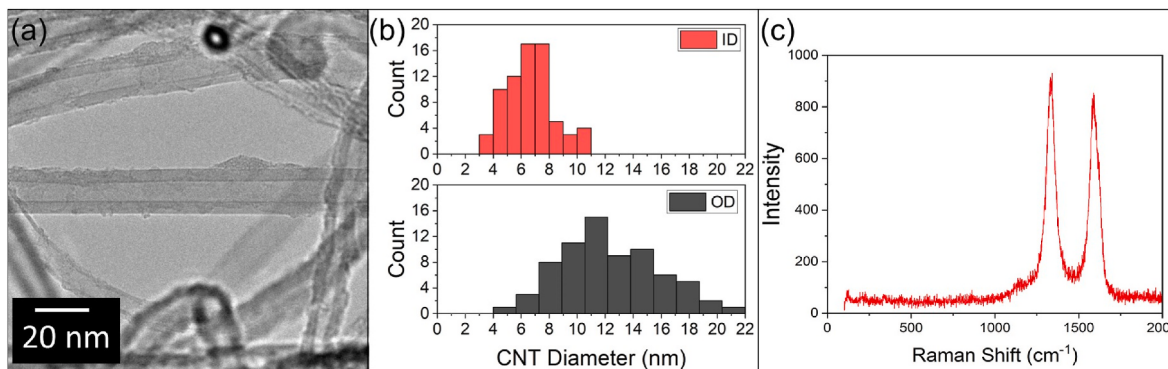


Fig. 9. Ex-situ analysis of CNT forests grown by in-situ ESEM CVD. (a) TEM image of CNTs synthesized by in-situ ESEM CVD. The walls of the MWCNTs are well aligned, and amorphous carbon is visible on the outer walls. (b) Histogram plot of inner diameter (ID) and outer diameter (OD) of CNTs measured from TEM images. (c) Raman spectra of CNT forests. (A colour version of this figure can be viewed online.)

CRediT authorship contribution statement

Ramakrishna Surya: Writing – review & editing, Writing – original draft, Visualization, Methodology, Investigation, Data curation. **Gordon L. Koerner:** Writing – review & editing, Writing – original draft, Investigation, Data curation. **Taher Hajilounezhad:** Data curation. **Kaveh Safavigerdini:** Visualization. **Martin Spies:** Data curation. **Prasad Calyam:** Supervision, Funding acquisition. **Filiz Bunyak:** Supervision, Funding acquisition. **Kannappan Palaniappan:** Supervision, Funding acquisition. **Matthew R. Maschmann:** Writing – review & editing, Supervision, Methodology, Funding acquisition, Formal analysis, Conceptualization.

Declaration of competing interest

The authors declare the following financial interests/personal relationships which may be considered as potential competing interests:

Matthew Maschmann reports financial support was provided by National Science Foundation. If there are other authors, they declare that they have no known competing financial interests or personal relationships that could have appeared to influence the work reported in this paper.

Acknowledgement

M.M., G.K., and T.H. acknowledge funding from NSF CMMI grant 1651538. M.M. and R.S. acknowledge funding from NSF CMMI grant 2026847. All authors acknowledge electron microscopy support from Dr. Dave Stalla and Dr. Xiaoqing He of the MU Electron Microscopy Core.

Appendix A. Supplementary data

Supplementary data to this article can be found online at <https://doi.org/10.1016/j.carbon.2024.119439>.

References

- [1] E.J. Garcia, B.L. Wardle, A.J. Hart, N. Yamamoto, Fabrication and multifunctional properties of a hybrid laminate with aligned carbon nanotubes grown in situ, *Compos. Sci. Technol.* 68 (9) (2008) 2034–2041.
- [2] S.S. Wicks, R.G. de Villoria, B.L. Wardle, Interlaminar and intralaminar reinforcement of composite laminates with aligned carbon nanotubes, *Compos. Sci. Technol.* 70 (1) (2010) 20–28.
- [3] M.R. Maschmann, G.J. Ehrlert, B.T. Dickinson, D.M. Phillips, C.W. Ray, G.W. Reich, J.W. Baur, Bioinspired carbon nanotube fuzzy fiber hair sensor for air-flow detection, *Adv. Mater.* 26 (20) (2014) 3230–3234.
- [4] M.R. Maschmann, B. Dickinson, G.J. Ehrlert, J.W. Baur, Force sensitive carbon nanotube arrays for biologically inspired airflow sensing, *Smart Mater. Struct.* 21 (9) (2012) 094024.
- [5] S.W. Lee, N. Yabuuchi, B.M. Gallant, S. Chen, B.-S. Kim, P.T. Hammond, Y. Shao-Horn, High-power lithium batteries from functionalized carbon-nanotube electrodes, *Nat. Nanotechnol.* 5 (7) (2010) 531–537.
- [6] T. Zhu, Y. Sha, H. Zhang, Y. Huang, X. Gao, M. Ling, Z. Lin, Embedding fe3c and fe3n on a nitrogen-doped carbon nanotube as a catalytic and anchoring center for a high-area-capacity li-s battery, *ACS Appl. Mater. Interfaces* 13 (17) (2021) 20153–20161.
- [7] R. Carter, B. Davis, L. Oakes, M.R. Maschmann, C.L. Pint, A high areal capacity lithium-sulfur battery cathode prepared by site-selective vapor infiltration of hierarchical carbon nanotube arrays, *Nanoscale* 9 (39) (2017) 15018–15026.
- [8] M. Park, B.A. Cola, T. Siegmund, J. Xu, M.R. Maschmann, T.S. Fisher, H. Kim, Effects of a carbon nanotube layer on electrical contact resistance between copper substrates, *Nanotechnology* 17 (9) (2006) 2294.
- [9] J. Xu, T.S. Fisher, Enhancement of thermal interface materials with carbon nanotube arrays, *Int. J. Heat Mass Tran.* 49 (9–10) (2006) 1658–1666.
- [10] M.R. Maschmann, Q. Zhang, F. Du, L. Dai, J. Baur, Length dependent foam-like mechanical response of axially indented vertically oriented carbon nanotube arrays, *Carbon* 49 (2) (2011) 386–397.
- [11] O. Yaglioglu, A. Cao, A.J. Hart, R. Martens, A. Slocum, Wide range control of microstructure and mechanical properties of carbon nanotube forests: a comparison between fixed and floating catalyst CVD techniques, *Adv. Funct. Mater.* 22 (23) (2012) 5028–5037.
- [12] A. Zbib, S.D. Mesarovic, E. Lilleodden, D. McClain, J. Jiao, D. Bahr, The coordinated buckling of carbon nanotube turfs under uniform compression, *Nanotechnology* 19 (17) (2008) 175704.
- [13] M.R. Maschmann, Q. Zhang, R. Wheeler, F. Du, L. Dai, J. Baur, In situ SEM observation of column-like and foam-like CNT array nanoindentation, *ACS Appl. Mater. Interfaces* 3 (3) (2011) 648–653.
- [14] A. Brieland-Shoultz, S. Tawfick, S.J. Park, M. Bedewy, M.R. Maschmann, J. W. Baur, A.J. Hart, Scaling the stiffness, strength, and toughness of ceramic-coated nanotube foams into the structural regime, *Adv. Funct. Mater.* 24 (36) (2014) 5728–5735.
- [15] B.F. Davis, X. Yan, N. Muralidharan, L. Oakes, C.L. Pint, M.R. Maschmann, Electrically conductive hierarchical carbon nanotube networks with tunable mechanical response, *ACS Applied Materials & Interfaces* 8 (41) (2016) 28004–28011.
- [16] S.B. Hutchens, L.J. Hall, J.R. Greer, In situ mechanical testing reveals periodic buckle nucleation and propagation in carbon nanotube bundles, *Adv. Funct. Mater.* 20 (14) (2010) 2338–2346.
- [17] A. Cao, P.L. Dickrell, W.G. Sawyer, M.N. Ghasemi-Nejhad, P.M. Ajayan, Super-compressible foamlke carbon nanotube films, *Science* 310 (5752) (2005) 1307–1310.
- [18] M.R. Maschmann, G.J. Ehrlert, S. Tawfick, A.J. Hart, J.W. Baur, Continuum analysis of carbon nanotube array buckling enabled by anisotropic elastic measurements and modeling, *Carbon* 66 (2014) 377–386.
- [19] S. Pathak, E.J. Lim, P. Pour Shahid Saeed Abadi, S. Graham, B.A. Cola, J.R. Greer, Higher recovery and better energy dissipation at faster strain rates in carbon nanotube bundles: an in-situ study, *ACS Nano* 6 (3) (2012) 2189–2197.
- [20] C.R. Oliver, W. Westrick, J. Koehler, A. Brieland-Shoultz, I. Anagnostopoulos-Politis, T. Cruz-Gonzalez, A.J. Hart, Robofurnace: a semi-automated laboratory chemical vapor deposition system for high-throughput nanomaterial synthesis and process discovery, *Rev. Sci. Instrum.* 84 (11) (2013) 115105.
- [21] E.R. Meshot, A.J. Hart, Abrupt self-termination of vertically aligned carbon nanotube growth, *Appl. Phys. Lett.* 92 (11) (2008) 113107.
- [22] E.R. Meshot, E. Verpoelen, M. Bedewy, S. Tawfick, A.R. Woll, K.S. Green, M. Hromalik, L.J. Koerner, H.T. Philipp, M.W. Tate, S.M. Gruner, A.J. Hart, High-speed in situ x-ray scattering of carbon nanotube film nucleation and self-organization, *ACS Nano* 6 (6) (2012) 5091–5101.
- [23] M. Bedewy, E.R. Meshot, M.J. Reinker, A.J. Hart, Population growth dynamics of carbon nanotubes, *ACS Nano* 5 (11) (2011) 8974–8989.
- [24] E.R. Meshot, A.J. Hart, Abrupt self-termination of vertically aligned carbon nanotube growth, *Appl. Phys. Lett.* 92 (11) (2008) 113107.
- [25] S.W. Pattinson, R.E. Diaz, N.A. Stelmashenko, A.H. Windle, C. Ducati, E.A. Stach, K.K. Koziol, In situ observation of the effect of nitrogen on carbon nanotube synthesis, *Chem. Mater.* 25 (15) (2013) 2921–2923.
- [26] V. Balakrishnan, M. Bedewy, E.R. Meshot, S.W. Pattinson, E.S. Polson, F. Laye, D. N. Zakharov, E.A. Stach, A.J. Hart, Real-time imaging of self-organization and mechanical competition in carbon nanotube forest growth, *ACS Nano* 10 (12) (2016) 11496–11504.
- [27] A. Yasuda, N. Kawase, W. Mizutani, Carbon-nanotube formation mechanism based on in situ tem observations, *J. Phys. Chem. B* 106 (51) (2002) 13294–13298.
- [28] M. Bedewy, B. Viswanath, E.R. Meshot, D.N. Zakharov, E.A. Stach, A.J. Hart, Measurement of the dewetting, nucleation, and deactivation kinetics of carbon nanotube population growth by environmental transmission electron microscopy, *Chem. Mater.* 28 (11) (2016) 3804–3813.
- [29] N.T. Dee, J. Li, A.O. White, C. Jacob, W. Shi, P.R. Kidambi, K. Cui, D.N. Zakharov, N.Z. Janković, M. Bedewy, et al., Carbon-assisted catalyst pretreatment enables straightforward synthesis of high-density carbon nanotube forests, *Carbon* 153 (2019) 196–205.
- [30] X. Huang, R. Farra, R. Schlögl, M.-G. Willinger, Growth and termination dynamics of multiwalled carbon nanotubes at near ambient pressure: an in situ transmission electron microscopy study, *Nano Lett.* 19 (8) (2019) 5380–5387.
- [31] R. Ma, L. Qiu, L. Zhang, D.-M. Tang, Y. Wang, B. Zhang, F. Ding, C. Liu, H.-M. Cheng, Nucleation of single-wall carbon nanotubes from faceted pt catalyst particles revealed by in situ transmission electron microscopy, *ACS Nano* 16 (10) (2022) 16574–16583.
- [32] X. Huang, R. Farra, R. Schlögl, M.-G. Willinger, Growth and termination dynamics of multiwalled carbon nanotubes at near ambient pressure: an in situ transmission electron microscopy study, *Nano Lett.* 19 (8) (2019) 5380–5387.
- [33] H. Yoshida, S. Takeda, T. Uchiyama, H. Kohno, Y. Homma, Atomic-scale in-situ observation of carbon nanotube growth from solid state iron carbide nanoparticles, *Nano Lett.* 8 (7) (2008) 2082–2086.
- [34] S. Jeong, J. Lee, H.-C. Kim, J.Y. Hwang, B.-C. Ku, D.N. Zakharov, A. Maruyama, E. A. Stach, S.M. Kim, Direct observation of morphological evolution of a catalyst during carbon nanotube forest growth: new insights into growth and growth termination, *Nanoscale* 8 (2016) 2055–2062.
- [35] W. Van Dorp, C.W. Hagen, A critical literature review of focused electron beam induced deposition, *J. Appl. Phys.* 104 (8) (2008) 10.
- [36] N. Miura, A.Y.A. Yamada, M.K.M. Konagai, Fabrication of sub-micron tungsten carbide (wcx)/amorphous carbon (ac) stacked junction by beam-induced reaction processes, *Jpn. J. Appl. Phys.* 36 (9A) (1997) L1275.
- [37] C. Soong, P. Woo, D. Hoyle, Contamination cleaning of tem/sem samples with the zone cleaner, *Microscopy Today* 20 (6) (2012) 44–48.
- [38] T. Hajilounezhad, D.M. Ajiboye, M.R. Maschmann, Evaluating the forces generated during carbon nanotube forest growth and self-assembly, *Materialia* 7 (2019) 100371.

- [39] T. Hajilounezhad, R. Bao, K. Palaniappan, F. Bunyak, P. Calyam, M.R. Maschmann, Predicting carbon nanotube forest attributes and mechanical properties using simulated images and deep learning, *npj Comput. Mater.* 7 (1) (2021) 1–11.
- [40] M.R. Maschmann, Integrated simulation of active carbon nanotube forest growth and mechanical compression, *Carbon* 86 (2015) 26–37.
- [41] N. Karaev, I. Rocco, B. Graham, N. Neverova, A. Vedaldi, C. Rupprecht, CoTracker: it Is Better to Track Together, 2023.
- [42] J. Carpena-Núñez, J.A. BoscoBoinik, S. Saber, R. Rao, J.-Q. Zhong, M. R. Maschmann, P.R. Kidambi, N.T. Dee, D.N. Zakharov, A.J. Hart, et al., Isolating the roles of hydrogen exposure and trace carbon contamination on the formation of active catalyst populations for carbon nanotube growth, *ACS Nano* 13 (8) (2019) 8736–8748.
- [43] M.R. Maschmann, G.J. Ehlert, S.J. Park, D. Mollenhauer, B. Maruyama, A.J. Hart, J.W. Baur, Visualizing strain evolution and coordinated buckling within cnt arrays by in situ digital image correlation, *Adv. Funct. Mater.* 22 (22) (2012) 4686–4695.
- [44] M.R. Maschmann, G.J. Ehlert, S. Tawfick, A.J. Hart, J.W. Baur, Continuum analysis of carbon nanotube array buckling enabled by anisotropic elastic measurements and modeling, *Carbon* 66 (2014) 377–386.
- [45] A.L. Kaiser, D.L. Lidston, S.C. Peterson, L.H. Acauan, S.A. Steiner, R. Guzman de Villoria, A.R. Vanderhout, I.Y. Stein, B.L. Wardle, Substrate adhesion evolves non-monotonically with processing time in millimeter-scale aligned carbon nanotube arrays, *Nanoscale* 13 (2021) 261–271.
- [46] J. Brown, T. Hajilounezhad, N.T. Dee, S. Kim, A.J. Hart, M.R. Maschmann, Delamination mechanics of carbon nanotube micropillars, *ACS Appl. Mater. Interfaces* 11 (38) (2019) 35221–35227.
- [47] N.T. Dee, M. Bedewy, A. Rao, J. Beroz, B. Lee, E.R. Meshot, C.A. Chazot, P. R. Kidambi, H. Zhao, T. Serbowicz, et al., In situ mechanochemical modulation of carbon nanotube forest growth, *Chem. Mater.* 31 (2) (2018) 407–418.
- [48] M. Bedewy, A.J. Hart, Mechanical coupling limits the density and quality of self-organized carbon nanotube growth, *Nanoscale* 5 (7) (2013) 2928–2937.
- [49] Y.A. Kim, H. Kakegawa, K. Fujisawa, D. Shimamoto, H. Muramatsu, J.H. Kim, Y. C. Jung, T. Hayashi, M. Endo, M. Terrones, M.S. Dresselhaus, Sensitive g-band Raman features for the electrical conductivity of multi-walled carbon nanotubes, *J. Nanosci. Nanotechnol.* 10 (6) (2010).
- [50] M. Bedewy, E.R. Meshot, H. Guo, E.A. Verploegen, W. Lu, A.J. Hart, Collective mechanism for the evolution and self-termination of vertically aligned carbon nanotube growth, *J. Phys. Chem. C* 113 (48) (2009) 20576–20582.